



# Influence of TiO<sub>2</sub> optical parameters in a slurry photocatalytic reactor: Kinetic modelling

A. Tolosana-Moranchel <sup>b</sup>, J.A. Casas <sup>b</sup>, J. Carbajo <sup>a</sup>, M. Faraldo <sup>a</sup>, A. Bahamonde <sup>a,\*</sup>

<sup>a</sup> Instituto de Catálisis y Petroleoquímica, ICP-CSIC, C/Marie Curie 2, 28049 Madrid, Spain

<sup>b</sup> Sección de Ingeniería Química, Facultad de Ciencias, C/Francisco Tomás y Valiente 7, Universidad Autónoma de Madrid, 28049 Madrid, Spain

## ARTICLE INFO

### Article history:

Received 20 April 2016

Received in revised form 20 June 2016

Accepted 25 June 2016

Available online 29 June 2016

### Keywords:

Photocatalysis

TiO<sub>2</sub>

Kinetic model

RTE

VRPA

## ABSTRACT

A kinetic model, based on a proposed reaction photo-mechanism and explicitly dependent on the volumetric rate of photon absorption (VRPA), has been performed and analyzed for the photocatalytic degradation of phenol in aqueous suspensions. UVA-vis simulated solar radiation and three commercial TiO<sub>2</sub> powder photocatalysts, with identical chemical structure but with different morphology and hydrodynamic particle size (P25 Aerioxide®, P25/20 VP Aeroperl® and P90 Aerioxide® provided by Evonik) have been used. The effect of TiO<sub>2</sub> hydrodynamic particle size on the optical coefficients has revealed that this property is playing an important role on the absorbed radiation evaluation. Radiation profiles inside the photoreactor were determined by solving the radiative transfer equation (RTE), and the corresponding kinetic parameters were obtained.

A comparative study of TiO<sub>2</sub> loading effect on calculated quantum efficiency ( $\eta$ ) revealed P25 was the most photo-efficient catalyst, whereas P25/20 reached similar efficiencies only when higher TiO<sub>2</sub> concentrations were used. On the contrary, P90 presented the lowest photo-efficiency with lower photodegradation rates despite absorbing more radiation.

The obtained kinetic model has been successfully validated by experimental data, being able to reproduce the evolution of phenol photodegradation at a wide range of catalyst concentrations for the three studied TiO<sub>2</sub>. In the experimental conditions of this work, low irradiation power conditions can be considered; after simplification, the model adopted a linear dependence on the volumetric rate of photon absorption; showing good agreement between predicted and experimental values, with root-square-mean errors below 5%.

© 2016 Elsevier B.V. All rights reserved.

## 1. Introduction

The heterogeneous photocatalytic process is based on the excitation of a catalytic solid, usually a broad bandgap semiconductor as TiO<sub>2</sub>, through the absorption of photons whose energy is equal or greater than their *band-gap* energy. Photo-generated electrons ( $e^-$ ) and holes ( $h^+$ ) will react with adsorbed molecules located at catalyst surface, leading to the oxidization of the organic matter by direct hole ( $h^+$ ) transfer or by indirect hydroxyl radical–oxidation ( $HO^\bullet$ ) [1]. In this context, solar photocatalytic processes contemplate the use of a natural light source such as the sun, environmental friendly, wherein the nanostructured TiO<sub>2</sub> catalysts can improve their final photoefficiency [2]. It is known that photocatalytic

processes are affected by different parameters which govern photo-oxidation rates, such as spectral distribution and intensity of the incident radiation, concentration and type of oxidizing agent, mass of catalyst, pH, etc. [1,3]. Therefore, to discriminate the overall performance of a photocatalyst is essential to know its intrinsic kinetic parameters to design new and improved photo-reactors. Then, a crucial requirement to develop novel photoreactors would be to build a kinetic model able to successfully reproduce the experimental rates obtained during photo-catalytic reaction [4]. Analysis of liquid-phase kinetics for titania powder suspensions have relied largely on Langmuir-Hinshelwood (LH) rate forms, which assumes equilibrated adsorption of reactants and implies the existence of a subsequent slow, rate-controlling surface step [5,6]. This kinetic model has demonstrated to well fit the concentration evolution of many organic pollutants in the photocatalytic literature [6]. However to carry out valuable comparison studies of the kinetic parameters among different labs, reactors and research works, it

\* Corresponding author.

E-mail address: [abahamonde@icp.csic.es](mailto:abahamonde@icp.csic.es) (A. Bahamonde).

| <b>Nomenclature</b>    |  | <b>Superscripts</b> |
|------------------------|--|---------------------|
| %A                     | Anatase crystalline phase percentage                                   | *                   |
| %R                     | Rutile crystalline phase percentage                                    | $\pm$               |
| ABS                    | Value of a absorbance spectrophotometric measurement                   | -                   |
| $a_V$                  | Interfacial area per unit suspension volume, $m^{-1}$                  | 0                   |
| BG                     | Band-gap, eV   | s                   |
| $C_{cat}$              | Mass catalyst concentration, $g\ cm^{-3}$                              |                     |
| $C_{Ph}$               | Molar phenol concentration, $mmol\ L^{-1}$                             |                     |
| $d_A$                  | Anatase mean diameter, nm  |                     |
| $d_{PHD}$              | Hydrodynamic particle diameter, $\mu m$                                |                     |
| $d_R$                  | Rutile mean diameter, nm   |                     |
| $e^a$                  | Volumetric rate of photon absorption, Einstein $cm^{-3}\ s^{-1}$       |                     |
| f                      | Spectral energy distribution of the lamp                               |                     |
| I                      | Specific radiation intensity, Einstein $cm^{-2}\ s^{-1}$               |                     |
| k                      | Kinetic constant, its units depend on the step considered              |                     |
| K                      | Equilibrium constant   |                     |
| LVRPA                  | Local volumetric rate of photon absorption, Einstein $cm^{-3}\ s^{-1}$ |                     |
| p                      | Function phase, dimensionless  |                     |
| q                      | Radiation flux, Einstein $cm^{-2}\ s^{-1}$                             |                     |
| R                      | Value of a reflectance spectrophotometric reflectance                  |                     |
| $r_g$                  | Surface rate of electron-hole generation, $mol\ cm^{-2}\ s^{-1}$       |                     |
| $(-r_{Ph})$            | Phenol photodegradation rate, $mmol\ L^{-1}\ min^{-1}$                 |                     |
| $r_{Fe(II)}$           | Fe(II) production rate, $mol\ L^{-1}\ min^{-1}$                        |                     |
| S                      | Relative to a subproduct species                                       |                     |
| $S_{BET}$              | Catalyst surface are (BET), $m^2\ g^{-1}$                              |                     |
| $S_{irr}$              | Area of the inlet radiation window, $cm^2$                             |                     |
| t                      | Time, min  |                     |
| $V_R$                  | Reactor volume, l  |                     |
| VRPA                   | Volumetric rate of photon absorption, Einstein $cm^{-3}\ s^{-1}$       |                     |
| <i>Greek letters</i>   |  |                     |
| $\alpha_1$             | Kinetic parameter, $mmol\ cm\ L^{-1}\ min^{-1}$                        |                     |
| $\alpha_2$             | Kinetic parameter, $cm^2\ s\ Einstein^{-1}$                            |                     |
| $\alpha_3$             | Kinetic parameter, $L\ mmol^{-1}$                                      |                     |
| $\beta$                | Extinction coefficient, $cm^{-1}$                                      |                     |
| $\eta$                 | Quantum efficiency, $mmol\ Einstein^{-1}$                              |                     |
| $\phi$                 | Quantum yield, $mol\ Einstein^{-1}$                                    |                     |
| $\bar{\phi}$           | Mean quantum yield, $mol\ Einstein^{-1}$                               |                     |
| $\kappa$               | Absorption coefficient, $cm^{-1}$                                      |                     |
| $\lambda$              | Wavelength, nm   |                     |
| $\mu$                  | Director cosine, $\mu = \cos\theta$                                    |                     |
| $\theta$               | Spherical coordinate, rad  |                     |
| $\Omega$               | Direction of radiation propagation                                     |                     |
| $\omega$               | Spectral albedo  |                     |
| <i>Subscripts</i>      |  |                     |
| 0                      | Initial value  |                     |
| $\lambda$              | Indicates a dependence on wavelength                                   |                     |
| Cat                    | Relative to catalyst   |                     |
| Exp                    | Experimental value   |                     |
| max                    | Maximum value  |                     |
| min                    | Minimum value  |                     |
| Mod                    | Simulated value  |                     |
| Ph                     | Relative to phenol   |                     |
| S                      | Relative to a subproduct   |                     |
| T                      | Total  |                     |
| $V_R$                  | Relative to reactor volume   |                     |
| <i>Special symbols</i> |  |                     |
| $\langle \rangle$      | Average value over a defined space                                     |                     |
| [ ]                    | Relative to concentration  |                     |

will be needed to pay attention to intensity of absorbed radiation in any single photoreactor, given that different parameters such as light intensity are grouped in LH model kinetic rate constants.

Therefore, to get a kinetic expression which can be employed within a great range of operating conditions and allow to scaling up the process, the model must have an explicit dependence on the absorbed radiation. Hence, volumetric rate of photon absorption (VRPA) inside photoreactor must be evaluated, since it is involved in the photocatalytic reaction by means of activation step [7]. In this context, the Radiative Transfer Equation (RTE) must be solved to determine the radiation field [8,9]. The RTE describes the radiation intensity at any position along a ray pathway through medium. Besides, it can be also applied to evaluate the radiation field in a heterogeneous system constituted by  $TiO_2$  particles suspended in aqueous suspensions.

Consequently, the aim of this work has consisted on developing an intrinsic kinetic model, where the explicit radiation absorption has been included to reproduce the experimental results obtained with three  $TiO_2$  powder catalysts in the photodegradation of phenol in aqueous suspensions using a slurry photoreactor with external surrounding radiation.  $TiO_2$  catalysts (P25 Aerioxide®, P25/20 VP Aeroperl® and P90 Aerioxide®) with identical chemical structure, but with different morphologic and hydrodynamic particle size were deliberately chosen to study the influence of catalyst loading on phenol photodegradation without any other collateral effect.

The main optical properties (extinction, absorption and scattering coefficients) which affect the overall photocatalytic behavior, have been determined, and its dependence on the hydrodynamic particle size in aqueous suspensions has been settled.

Finally, a comparison study of calculated quantum efficiency for different  $TiO_2$  loading was also analyzed to establish the most photo-efficient catalyst under the studied conditions.

## 2. Experimental section

### 2.1. Photocatalysts

Photocatalytic experiments were performed using three  $TiO_2$  commercial catalysts: P25 Aerioxide®, P90 Aerioxide® and P25/20 VP Aeroperl®, all of them provided by Evonik Company.

Analytical grade phenol was purchased from Panreac. All reagents used for chromatographic analyses: (Milli-Q water, Orthophosphoric acid, methanol) were HPLC grade.

### 2.2. Photocatalysts characterization

Catalysts structural characterization were performed with a X polycrystal PANalytical X'Pert PRO using nickel-filtered  $Cu K\alpha$  ( $1.541874\text{ \AA}$ ) radiation operating at  $40\text{ kV}$  and  $40\text{ mA}$ , with a  $0.02^\circ$  step size and accumulating a total of  $50\text{ s}$  per point, crystal size was estimated by employing the Scherrer equation [10].

Nitrogen adsorption-desorption isotherms measurements were obtained at  $77\text{ K}$  in a Micrometrics Tristar automatic apparatus,

samples were previously outgassed overnight at 413 K to a vacuum of  $<10^{-4}$  Pa to ensure a dry and clean surface free from any loosely adsorbed species and, specific surface areas were determined by the BET method [11].

UV-vis diffuse reflectance spectra of the photocatalytic powders were using Agilent Cary 5000 spectrophotometer equipped with an integrating sphere. Band-gap was determined by the equation  $\alpha \propto h \times v = A \times (hv - Eg)^{n/2}$  [12].

Laser Diffraction (LD) measurements were performed to characterize the hydrodynamic particle size distribution of TiO<sub>2</sub> aggregates in aqueous suspensions using Mastersizer S by Malvern Instruments.

Finally, the optical properties of the catalyst suspensions were determined with a Agilent Cary 5000 UV-vis spectrophotometer following the methodology proposed by Cassano et al. [13–15]. Extinction measurements were carried out in transmission mode, placing a narrow slit before detector to reduce the collection of out-scattered rays. The sample cell, made of quartz (optical length, 2 mm) was located as far as possible from detector slit (Milli-Q water was used as baseline). The experimental setup for absorbance and reflectance measurements was constituted by the quartz sample cell fixed to a magnetic stirrer placed in the inlet and outlet of the integrating sphere, respectively (Milli-Q water and PTFE-Spectralon® were used as reference, respectively). Measurements were performed on freshly prepared and non-sonicated suspensions at different catalyst loadings. Under all the studied conditions, the suspensions were rather stable and fairly reproducible during the three consecutive measurements carried out.

### 2.3. Photocatalytic activity

Photodegradation runs were carried out in a stirred 1 L Pyrex semi-continuous slurry photoreactor [16] set in a Multirays apparatus (Helios Italquartz) at atmospheric pressure and room temperature (details about the reactor are shown in Supporting Information Table 1). The cylindrical reactor (76 mm i.d.) was enclosed by 10 fluorescent lamps of 15 W each (6 Black Light Blue UVA lamps and 4 day-light lamps) surrounded by an aluminum reflecting surface. This set of lamps was used to work with a total radiant flux in the UV-A range closed to the typical average solar UV flux values, found to be 30 W<sub>UVA</sub> m<sup>-2</sup> [17]. Total irradiance, 38 W m<sup>-2</sup>, was measured by a Kipp & Zonen model CUV-4 broadband UV radiometer in UV-A range (306–383 nm). Furthermore, radiation flow entering to the reactor and provided by the 6 Black Light Blue UVA lamps was determined by carrying out a potassium ferrioxalate actinometry [18].

Phenol photo-oxidation runs were carried out at the following operating conditions: atmospheric pressure, initial concentration of 50 mg L<sup>-1</sup> phenol at natural pH 6, with a continuous oxygen flow of 75 Ncm<sup>3</sup> min<sup>-1</sup>. Different TiO<sub>2</sub> catalysts loadings (25–150 mg L<sup>-1</sup>) were also studied at the same operating conditions. First, the reactant mixture with the corresponding catalyst loading were premixed in dark conditions during 30 min to guarantee homogeneous mixing in the photoreactor, to take into account the adsorption equilibrium stage. After that, photocatalytic runs started by turning on all lamps, and small portions of the solutions were extracted at selected times to follow the reaction.

Phenol and aromatic intermediates were identified and quantified by means of High Performance Liquid Chromatography HPLC (Varian 920 LC) with photo-diode array detector. A Nucleosil C18 5 μm column (15 cm long, 4.6 mm diameter) was used as stationary phase at 40 °C. Mobile phase flow was 0.8 mL min<sup>-1</sup> and 20/80% v/v methanol/acidic water (0.1% phosphoric acid) mixture were used as solvent.

## 3. Results and discussion

### 3.1. Catalyst properties

In Table 1 are summarized the main physico-chemical properties of these three studied TiO<sub>2</sub> catalysts. From XRD measurements, all of them present similar crystallinity, with two titania crystal phases, approximately 88–85% anatase and 12–15% rutile respectively. Although P90 presented slightly lower anatase and rutile crystal sizes than P25 and P25/20 catalysts, the crystal structure do not seem to affect their band-gap values. Their specific surface areas ( $S_{BET}$ ) revealed that both P25 and P25/20 catalyst presented the same area (54 m<sup>2</sup> g<sup>-1</sup>), whereas P90 shows a higher surface area (81 m<sup>2</sup> g<sup>-1</sup>).

These Evonik commercial titania materials are characterized by unique macroporosity as correspond to non-porous type II isotherm [19], which must be only related to agglomerates, aggregates, small particles, or inter-particular spaces, given that their surface areas exactly agrees with their external surface areas (as it can be seen in Table 1), where total pore volume only corresponds to inter-particle spaces.

It is essential to understand TiO<sub>2</sub> particle interactions over a broad range of physicochemical conditions, given that aggregation of titania particles in the aqueous suspensions could have an important effect on final photocatalytic activity. In this context, the hydrodynamic particle size measured by Laser Diffraction (LD) will be indicative of the apparent size of the dynamic hydrated/solvated particle; hence the terminology, *hydrodynamic diameter* [20,21]. Considering that photocatalytic particles should favor efficient absorption of incident photons to avoid reduction of photodegradation rate due to lack of light [22], identifying the hydrodynamic particle size of TiO<sub>2</sub> particles in aqueous media must be crucial to understand photocatalyst phenomena.

The hydrodynamic particle size values determined by Laser Diffraction measurements are shown in Table 1. P25/20 sample has presented a significantly larger sizes than P25 and P90, being its hydrodynamic mean diameter value about 10 times higher. However, although P90 and P25 presented particle sizes of the same order of magnitude, P90 hydrodynamic particle size was more than double than TiO<sub>2</sub> P25. These important differences found in titania particles behavior in aqueous suspensions could well lead to a very different photocatalytic performance, in spite of the similarity found among the rest of their physico-chemical properties.

Therefore, these studied TiO<sub>2</sub> catalysts present a set of common structural and surface properties which will allow evaluating how photocatalytic activity could be independently affected by their hydrodynamic particle sizes.

### 3.2. Optical properties

The optical properties of these studied TiO<sub>2</sub> catalysts were carried out in the range of used lamps, from 345 to 405 nm, following the methodology proposed by Cabrera et al. [14], and Satuf et al. [15]. Extinction coefficients were calculated from conventional spectrophotometric measurements of corresponding TiO<sub>2</sub> suspensions. Thus, for each wavelength ( $\lambda$ ) and each path cell (L), the extinction coefficient is:

$$\beta_\lambda = \frac{2.303 \text{Abs}_\lambda}{L} \quad [\text{cm}^{-1}] \quad (1)$$

Subsequently, the specific extinction coefficients ( $\beta^*_\lambda$ ) for each catalyst were obtained by means of linear regressions of  $\beta_\lambda$  data vs  $C_{\text{cat}}$ .

It was also necessary to carry out transmittance or reflectance spectrophotometric measurements by means of an integrating sphere which allowed collect not only the non-absorbed radia-

**Table 1**Physico-chemical properties of TiO<sub>2</sub> catalysts.

| Catalyst | % A | % R | d <sub>A</sub> (nm) | d <sub>R</sub> (nm) | S <sub>BET</sub> (m <sup>2</sup> g <sup>-1</sup> ) | A <sub>external</sub> (m <sup>2</sup> g <sup>-1</sup> ) | V <sub>Pore</sub> (cm <sup>3</sup> g <sup>-1</sup> ) | d <sub>HDP</sub> (μm) | BG (eV) |
|----------|-----|-----|---------------------|---------------------|--|---|--|-----------------------|---------|
| P25      | 85  | 15  | 21.5                | 33.0                | 54   | 54  | 0.65   | 1.2                   | 3.2     |
| P90      | 87  | 13  | 17.3                | 31.5                | 81   | 81  | 0.50   | 2.6                   | 3.2     |
| P25/20   | 88  | 12  | 21.0                | 33.0                | 54   | 54  | 0.26   | 11.3                  | 3.2     |

A: Anatase; R: Rutile; HDP: Hydrodynamic particle size.

tion, but also the forward-scattered radiation to determine the absorption coefficient ( $\kappa_\lambda$ ). Nevertheless, these measures had to be corrected considering the scattered radiation in other directions. Then, the absorption coefficient was calculated by solving the Radiative Transfer Equation (RTE) (Eq. (2)) in the sample cell, where TiO<sub>2</sub> aqueous suspensions are contained.

$$\frac{dI_\lambda(s, \Omega)}{ds} + \underbrace{\kappa_\lambda I_\lambda(s, \Omega)}_{\text{Absorption}} + \underbrace{\sigma_\lambda I_\lambda(s, \Omega)}_{\text{Out-scattering}} = \underbrace{\frac{\sigma_\lambda}{4\pi} \int_{\Omega'=4\pi} p(\Omega' \rightarrow \Omega) I_\lambda(s, \Omega') d\Omega'}_{\text{In-scattering source term}} \quad (2)$$

In the case of the studied set-up (a sample cell irradiated by a collimated-unidirectional beam) a one-dimensional-one-directional radiation transport model can be applied to attain scattering of the system (mathematical derivation of a 1-dimensional, 1-directional radiation model can be found in the Supporting information). Theoretical values of the absorption coefficients can be determined from the proposed model [14,15]. The RTE model takes the following form:

$$\mu \cdot \frac{dI_\lambda(x, \mu)}{dx} + \beta_\lambda \cdot I_\lambda(x, \mu) = \frac{\beta_\lambda - \kappa_\lambda}{2} \int_{\mu'=-1}^{\mu'=1} p(\mu, \mu') \cdot I_\lambda(x, \mu) \cdot d\mu' \quad (3)$$

where  $\mu = \cos \theta$ . An isotropic phase function has been assumed in this work, as one of the most adequate to describe the scattering properties of a semiconductor catalysts such as titania [9,23,24] where  $p(\mu, \mu') = 1$ . The two boundaries conditions at  $x=0$  and at  $x=L$ , required for this model, depend on the kind of spectrophotometric measures carried out [8,13,14].

A discretization mathematical algorithm, known as Discrete Ordinate Method (DOM), has been applied to obtain the numerical solution of the RTE. This method consists on the transformation of the integral-differential RTE into a system of algebraic equations, which describes transport of photons in such way that they can be solved following the direction of propagation, starting from the values provided by the boundary conditions [8,9].

Absorption coefficient and its specific absorption coefficient ( $\kappa^*_\lambda$ ) were obtained [14,15] by comparison of experimental information with model predictions, and minimizing errors. Finally, the specific scattering coefficient can be determined as,

$$\sigma_\lambda^* = \beta_\lambda^* - \kappa_\lambda^* \quad (4)$$

Results of the specific extinction, specific absorption and specific scattering coefficients for each TiO<sub>2</sub> catalyst are shown in Fig. 1. It can be noticed that values obtained for P25 and P90 samples are far higher than those obtained for P25/20 catalyst, despite all of them present similar responses over all investigated wavelength range. From Fig. 1C, the absorption coefficients undergo an important decrease along wavelength values until becoming null above

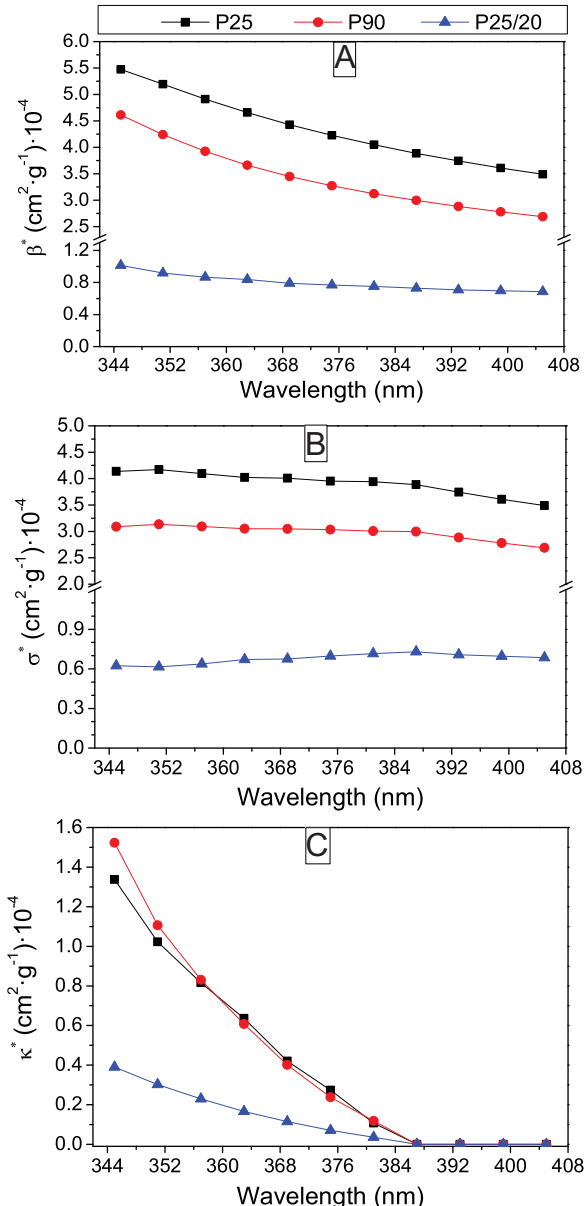
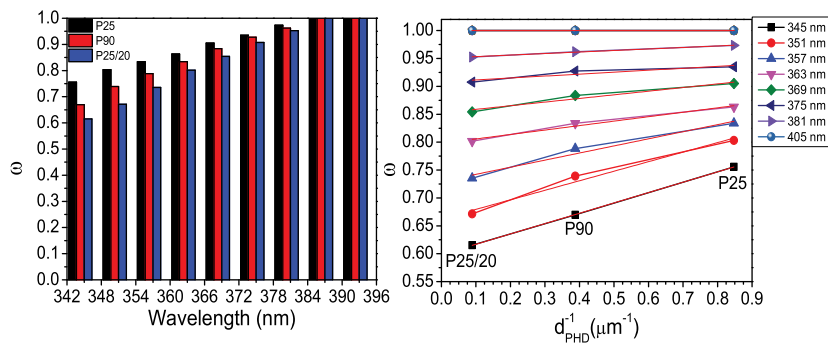


Fig. 1. Optical properties of TiO<sub>2</sub> catalysts (P25, P90 and P25/20). (A) Extinction Coefficient; (B) Scattering Coefficient; (C) Absorption Coefficient.

390 nm, which exactly corresponds to the bandgap of TiO<sub>2</sub> semiconductors.

On the other side, P25 has showed the highest scattering coefficients whereas P25/20 has presented the lowest values. This could be well related to the hydrodynamic particle size given that P25 and P25/20 with identical structural and surface properties, presented the wider and smaller hydrodynamic particle diameters, respectively. To go deepening into the understanding of hydrodynamic particle size effect on scattering, the ratio of the scattering to the extinction coefficients, usually called albedo ( $\omega$ ), has been com-



**Fig. 2.** Influence of wavelength (A) and hydrodynamic particle size (B) on the albedo coefficient ( $\omega$ ).

**Table 2**

Scheme of the proposed phenol photodegradation mechanism over  $\text{TiO}_2$  catalysts.

|                   |   |                                     |
|-------------------|---|-------------------------------------|
| Activation        | $\text{TiO}_2 \xrightarrow{h\nu} \text{TiO}_2 + e^- + h^+$  | [1]                                 |
| Adsorption        | $O_2^{+} + \text{Ti}^{IV} + H_2O \leftrightarrow O_LH^- + \text{Ti}^{IV} - OH^-$<br>$\text{Ti}^{IV} + H_2O \leftrightarrow \text{Ti}^{IV} - H_2O$<br>$Site + Ph \leftrightarrow Site Ph$<br>$HO + \text{Ti}^{IV} \leftrightarrow \text{Ti}^{IV} HO$   | [2a]<br>[2b]<br>[3]<br>[4]          |
| Recombination     | $e^- + h^+ \rightarrow heat$  | [5]                                 |
| Holes trapping    | $\text{Ti}^{IV} - OH^- + h^+ \rightarrow \text{Ti}^{IV} HO$<br>$\text{Ti}^{IV} - H_2O + h^+ \rightarrow H^+ + \text{Ti}^{IV} HO$  | [6a]<br>[6b]                        |
| Electron trapping | $\text{Ti}^{IV} Ph + h^+ \leftrightarrow \text{Ti}^{IV} Ph^+$<br>$e^- + \text{Ti}^{IV} \leftrightarrow \text{Ti}^{IVII}$  | [7]<br>[8a]                         |
| Hydroxyl attack   | $O_2 + \text{Ti}^{IVII} \leftrightarrow \text{Ti}^{IV} - O_2^-$<br>$\text{Ti}^{IV} HO^- + \text{Ti}^{IV} Ph \rightarrow \text{Ti}^{IV} + \text{Ti}^{IV}$<br>$HO + \text{Ti}^{IV} Ph \rightarrow \text{Ti}^{IV} S$<br>$\text{Ti}^{IV} HO^- + Ph \rightarrow \text{Ti}^{IV} + S$<br>$HO + Ph \rightarrow S$ | [8b]<br>[9]<br>[10]<br>[11]<br>[12] |

pared in Fig. 2; where a linear dependence with the inverse of the hydrodynamic particle size was always observed for these three  $\text{TiO}_2$  catalysts. Lower hydrodynamic particle diameters provoke high particle dispersions which would lead to high albedo coefficient values. Therefore, could be concluded that P25 presented a major proportion of scattering coefficient than the other two studied  $\text{TiO}_2$  catalysts.

### 3.3. Kinetic model

The phenol photocatalytic mineralization mechanism used in this work is based on that proposed by Turchis and Ollis [25], and Alfano et al. [26] (see Table 2); where the following steps are considered: activation by photons absorption to form the electron-hole pair (1), adsorption of water, the organic compound, and hydroxyl radical on the catalyst surface (2), recombination of electron and holes formed (3), hole trapping (4), electron trapping (5), and hydroxyl attack ( $\text{HO}^\bullet$ ), where adsorbed and non-adsorbed hydroxyl radicals can react not only with the adsorbed organic compound on the catalyst surface, but also with the organic compounds in aqueous solution (Eqs. (9)–(12)).

Thus, the following kinetic expression was obtained from the above reaction pathway assuming the kinetic steady state for the  $\text{HO}^\bullet$  and holes generation (see Appendix A):

$$(-r_{Ph})_{V_R} = S_{BET}C_{cat}\alpha_1 \frac{\alpha_{3,Ph}C_{Ph}}{(\alpha_{3,Ph}C_{Ph} + 1)} \left\{ -1 + (\sqrt{1 + \frac{\alpha_2e^a(x)}{S_{BET}C_{cat}}}) \right\} \quad (5)$$

To determine all kinetic parameters: first, incident radiation flux for each wavelength was calculated; secondly, the radiative transfer equation (RTE) was solved by using DOM with the corresponding boundaries conditions. Following, once the radiation intensities were determined, the volumetric rate of photon absorption (VRPA) could be calculated [9].

### 3.4. Volumetric rate of photon absorption (VRPA) and quantum efficiencies for phenol degradation

Ferrioxalate actinometry runs were carried out to estimate inlet radiation fluxes into the photoreactor used in this work [18], which were calculated by applying reactor mass balance [27]. Then, total inlet radiation flux was determined as,

$$q_T^0 = \langle r_{Fe(II),0}(x, t) \rangle_{V_R} \cdot \frac{V_R}{\phi_\lambda \cdot S_{Irr}} \quad (6)$$

where  $\phi_\lambda = 1.2$ , for all studied wavelength range. As  $q_T^0$  is the total flux, a discretization must be performed to calculate the intensities entering the reactor for each wavelength [27,28]:

$$I_\lambda^0 = \frac{q_T^0 \cdot f_\lambda}{\pi} = \frac{q_\lambda^0}{\pi} \quad (7)$$

where  $f_\lambda$  is the spectral energy distribution of the lamp obtained from the relative intensities of the lamp emission spectrum and the following normalization condition:  $q_\lambda^0 = \int_\lambda q_\lambda^0 d\lambda$  [27].

Once inlet spectral intensities were known, and the RTE was solved by using DOM, the radiation field could be evaluated [8]. One-dimensional-one-directional radiation transport model was applied (Eq. (8)) because azimuthal symmetry was assumed as a considerable percentage of diffuse radiation was entering into the reactor due to the surrounding reflective surface [29]. A schematic representation of the radiation field inside the photoreactor is depicted in Fig. 1 of Supporting Information.

$$\begin{aligned} & \mu \cdot \frac{dI_\lambda(x, \mu)}{dx} + (\kappa_\lambda + \sigma_\lambda) \cdot I_\lambda(x, \mu) \\ &= \frac{\sigma_\lambda}{2} \int_{\mu'=-1}^{\mu'=1} p(\mu, \mu') \cdot I_{\lambda,}(x, \mu) \cdot d\mu' \end{aligned} \quad (8)$$

where  $\kappa_\lambda + \sigma_\lambda = \beta_\lambda$ . An isotropic phase function has been taken again [9,14]. In this case the boundaries conditions needed to solve the RTE are:

$$\begin{aligned} I_\lambda(x=0, \mu) &= I_\lambda^0 \quad \mu > 0 \\ I_\lambda(x=L, \mu) &= I_\lambda^0 \quad \mu < 0 \end{aligned} \quad (9)$$

After calculating the radiation intensities, the local volumetric rate of photon absorption (LVRPA,  $e^a(x)$ ) in each point of the photoreactor, could be determined by the following equation:

$$e^a(x) = \int_{\lambda_{min}}^{\lambda_{max}} \kappa_\lambda 2\pi \int_{\mu=-1}^{\mu=1} I_\lambda(x, \mu) d\mu d\lambda \quad \frac{\text{Einstein}}{\text{cm}^3 \cdot \text{s}} \quad (10)$$

Before obtaining the volumetric rate of photon absorption (VRPA,  $e^a$ ), the average volumetric photon rate over the suspension

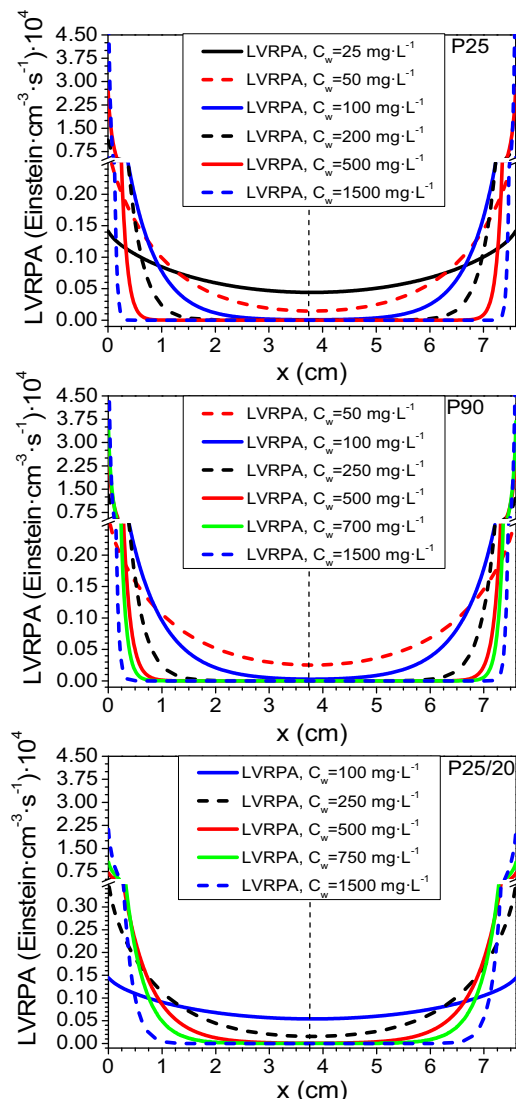


**Fig. 3.** Local Volumetric Rates of Photon Absorption (LVRPA) at different catalysts concentrations, for P25, P90 and P25/20.

bulk must be calculated by integrating the LVRPA values obtained for each point.

In Fig. 3 LVRPA profiles inside the reactor thickness ( $x$ ) are depicted for each catalyst, analyzing the effect of  $\text{TiO}_2$  catalyst loading.

On increasing  $\text{TiO}_2$  catalyst loading in this studied photoreactor two effects can be observed: higher attenuation in the center of photoreactor joined to increased absorption of radiation near the walls. Attenuation values were significantly higher when P25 and P90 were employed as a consequence of their significantly higher absorption and scattering coefficients compared to those found for P25/20 catalyst (see Fig. 1). Finally, in the center of photoreactor almost null absorbed radiation could be observed when  $0.1 \text{ g L}^{-1}$  of P25 or P90 catalysts were used, whereas higher P25/20 concentrations ( $0.5 \text{ g L}^{-1}$ ) were necessary to reach the same conditions.

A comparison study of the average VRPA evolution as a function of the catalyst concentration for the studied catalysts is showed in Fig. 4. Important increases of VRPA with rising catalyst loading were observed in all cases until  $0.2 \text{ g L}^{-1}$  of  $\text{TiO}_2$  concentration. Whereas almost any difference was found for both P25 and P90 ( $0.15\text{--}0.2 \text{ g L}^{-1}$ ), higher catalyst loading ( $0.6 \text{ g L}^{-1}$ ) was required to get similar VRPA values in the case of P25/20.

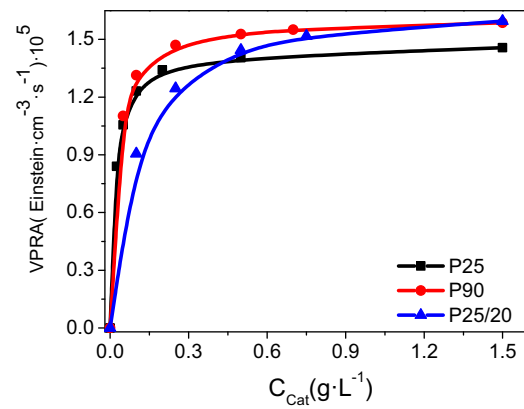


**Fig. 4.** Effect of different  $\text{TiO}_2$  catalyst loading on mean Volumetric Rate of Photon Absorption inside the photoreactor.

**Table 3** presents the effect of catalyst concentration ( $C_{\text{Cat}}$ ) and VRPA on the initial phenol photo-oxidation rate ( $-r_{\text{Ph},0}$ ), for each  $\text{TiO}_2$ , in this studied photoreactor. The highest initial phenol photo-oxidation rate ( $3.6 \times 10^{-3} \text{ mmol L}^{-1} \text{ min}^{-1}$ ) was obtained at high concentrations of P25/20 catalyst, as a consequence of its low extinction and scattering coefficients that allowed the use of higher catalyst loadings at the same time that higher VRPA values were reached. Meanwhile, at lower catalyst concentrations, whatever the VRPA value was, higher reaction rates were always arisen for both P25 and P90 catalyst. However, it can be noted the maximum initial photodegradation rate reached by P90 ( $2.9 \times 10^{-3} \text{ mmol L}^{-1} \text{ min}^{-1}$ ) was lower than that reached by P25 ( $3.3 \times 10^{-3} \text{ mmol L}^{-1} \text{ min}^{-1}$ ), in spite of P25 absorbed lower radiation than P90. Therefore, for the reactor employed in this study it can be considered as optimal catalyst concentration, 0.3, 0.2 and  $0.6 \text{ g L}^{-1}$  for P25, P90 and P25/20, respectively, for the photoreactor used in this work.

In the case of P90 catalyst, initial reaction rate barely depends on catalyst concentration. Besides, the total amount of absorbed photons resulted invariable for P90 concentrations over  $0.1 \text{ g L}^{-1}$ , despite most of the radiation was absorbed close to the walls (see Figs. 3 and 4), that could be explained because photons absorbed near the walls are able to generate so many effective carriers as when they are absorbed in the bulk, given that at lower irradiation power conditions, photodegradation rate linearly depends on VRPA.

Comparison of different  $\text{TiO}_2$  intrinsic activity and their corresponding efficiency in the use of photons, were carried out considering the known parameter quantum efficiency ( $\eta$ ), that was calculated for each catalyst from relation between initial reaction rate of phenol photodegradation ( $-r_{\text{Ph},0}$ ) and the average volumetric rate of absorbed photons ( $e^a$ ) [27].

Considering the initial phenol reaction rate is:

$$(-r_{\text{Ph},0}) = \lim_{t \rightarrow 0} -\frac{\Delta C}{\Delta t} \quad (11)$$

Quantum efficiency can be calculated as,

$$\eta = \frac{(-r_{\text{Ph},0})}{e^a} \quad (12)$$

The effect of catalyst loading on the calculated quantum efficiency is shown in Fig. 5, where the highest photo-efficiency was achieved when a great amount of P25/20 ( $0.6 \text{ g L}^{-1}$ ), or low P25 catalyst concentration, was used ( $0.1 \text{ g L}^{-1}$ ). However, P90 presented the lowest catalytic photoefficiency providing lower photo-oxidation rates in spite of absorbing more photons; what points to a higher likelihood of suffering recombination of the

**Table 3**

Influence of catalyst concentration on initial rate of phenol photodegradation and VRPA, for P25, P90 and P25/20.

| P25                                       |   |  | P90                                       |   |  | P25/20                                    |   |  |
|---|---|--|---|---|--|---|---|--|
| C <sub>Cat</sub><br>(mg L <sup>-1</sup> ) | −r <sub>Ph,0</sub> × 10 <sup>3</sup><br>(mmol L <sup>-1</sup> min <sup>-1</sup> ) | VRPA × 10 <sup>5</sup><br>(Einstein cm <sup>-3</sup> s <sup>-1</sup> ) | C <sub>Cat</sub><br>(mg L <sup>-1</sup> ) | −r <sub>Ph,0</sub> × 10 <sup>3</sup><br>(mmol L <sup>-1</sup> min <sup>-1</sup> ) | VRPA × 10 <sup>5</sup><br>(Einstein cm <sup>-3</sup> s <sup>-1</sup> ) | C <sub>Cat</sub><br>(mg L <sup>-1</sup> ) | −r <sub>Ph,0</sub> × 10 <sup>3</sup><br>(mmol L <sup>-1</sup> min <sup>-1</sup> ) | VRPA × 10 <sup>5</sup><br>(Einstein cm <sup>-3</sup> s <sup>-1</sup> ) |
| 25  | 0.92  | 0.84   | 50  | 1.03  | 1.10   | 100                                       | 1.19  | 0.91   |
| 50  | 1.45  | 1.06   | 100                                       | 1.95  | 1.31   | 250                                       | 2.16  | 1.24   |
| 100                                       | 2.55  | 1.23   | 250                                       | 2.82  | 1.47   | 500                                       | 3.09  | 1.44   |
| 200                                       | 2.73  | 1.34   | 500                                       | 2.52  | 1.53   | 750                                       | 3.38  | 1.52   |
| 500                                       | 3.11  | 1.40   | 700                                       | 2.90  | 1.55   | 1500                                      | 3.49  | 1.59   |
| 1500                                      | 3.30  | 1.46   | 1500                                      | 2.86  | 1.59   |   |   |  |

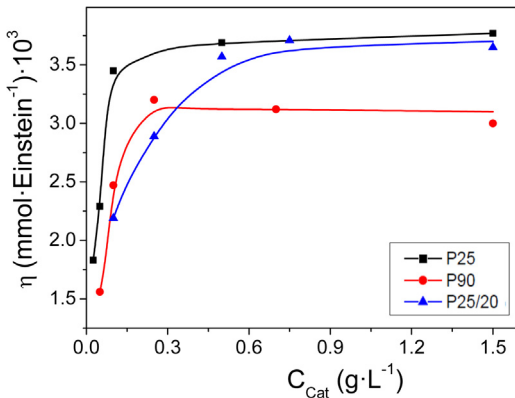


Fig. 5. Calculated quantum efficiency for different TiO<sub>2</sub> catalyst concentration.

formed electron-holes pairs, which can be detrimental for the overall photocatalytic efficiency.

### 3.5. Kinetic parameters

Experimental results of phenol photodegradation were compared with the average reaction rates in whole reactor volume to estimate or predict the kinetic parameters for the proposed model (Eq. (5)), applying non-linear regressions based on Lever-Marquardt algorithm.

Total root-square-mean errors (RSME) were calculated [29] to evaluate the mathematical goodness of fit. Very good correlations between predicted and experimental values can be seen in Fig. 6, where phenol evolution as a function of catalysts loading is followed for the three studied titania catalysts. Moreover, estimated values of kinetic parameters for each TiO<sub>2</sub> catalyst with their 95% confidence intervals and their corresponding errors are shown in Table 4.

Concluding, the proposed kinetic model is able to simulate with very good accuracy the obtained experimental results of phenol photodegradation using these TiO<sub>2</sub> catalysts.

However, for some parameters ( $\alpha_3$ ) the values of confidence intervals are close to the corresponding parameter itself. This could be due to possible interactions among the high number of parameters acting in the kinetic model proposed, what means there is at least a parameter to spare. Thus, the model was simplified assuming that the experiments were carried out under low irradiation conditions.

When the reactor operates at low values of irradiation power, originates low rate of photon absorption, consequently, the term containing VRPA becomes lower,  $\frac{\alpha_2 e^a}{S_{BET} C_{cat}} \ll 1$ , and the square root can be simplified by the first term of the Taylor series expansion

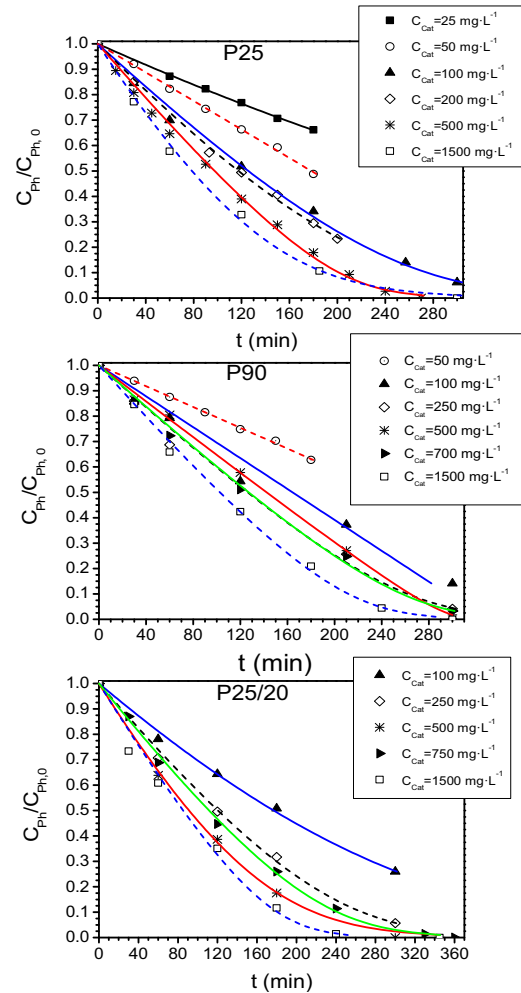


Fig. 6. Evolution of phenol photodegradation on P25, P90 and P25/20, at different catalysts concentrations (Lines correspond to fittings from experimental data).

$(\sqrt{1+x} = 1 + x/2)$ , where the model takes the following form, which shows a linear dependence on the average of the VRPA [30]:

$$(-r_{Ph})_{VR} = \underbrace{a_1 a_2}_{a} (e^a(x)) \frac{a_{3,Ph} C_{Ph}}{(a_{3,Ph} C_{Ph} + 1)} \quad (13)$$

The kinetic parameters estimated for this simplified model (Table 5) presented smaller associated errors, what permits to accept the simplification of the model is adequate to reproduce the obtained experimental values accurately. This conclusion is supported by Fig. 7 under low radiation power conditions, where the good correlation between the prediction of the model and the experimental data can be seen, especially taking into account that there is no explicit dependence on catalyst concentration.

**Table 4**

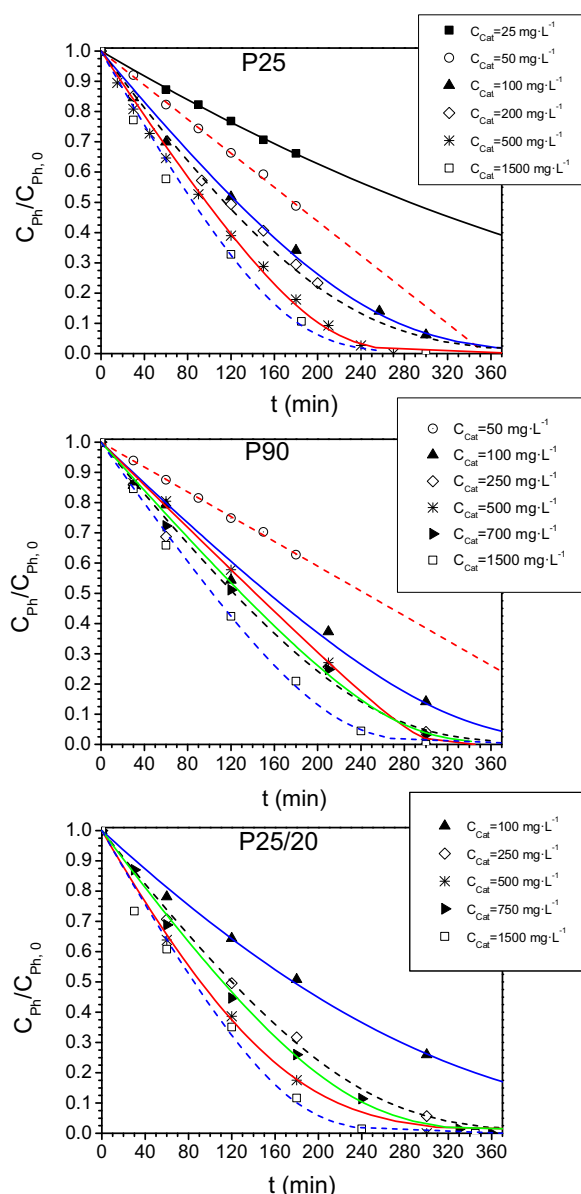
Kinetic parameters calculated by means of nonlinear multiple regressions.

| Catalyst | $\alpha_1$ (mmol cm L <sup>-1</sup> min <sup>-1</sup> ) |                 | $\alpha_2$ (cm <sup>2</sup> s Einstein <sup>-1</sup> ) |                 | $\alpha_3$ (L mmol <sup>-1</sup> ) |                 | RSME (%) |
|----------|---|-----------------|--|-----------------|------------------------------------|-----------------|----------|
|          | Value   | Confidence Int. | Value  | Confidence Int. | Value                              | Confidence Int. |          |
| P25      | 8.79  | ±2.22           | 18.49  | ±2.73           | 5.45                               | ±2.39           | 4.37     |
| P90      | 1.24  | ±1.03           | 39.44  | ±7.97           | 13.33                              | ±9.58           | 4.68     |
| P25/20   | 4.64  | ±1.33           | 30.96  | ±4.65           | 6.23                               | ±2.55           | 4.63     |

**Table 5**

Kinetic parameters calculated by means of nonlinear multiple regressions for the proposed kinetic in which a low irradiant power is considered.

| Catalyst | $\alpha$ (mmol Einstein <sup>-1</sup> ) |                 | $\alpha_3$ (L mmol <sup>-1</sup> ) |                 | RSME (%) |
|----------|---|-----------------|------------------------------------|-----------------|----------|
|          | Value                                   | Confidence Int. | Value                              | Confidence Int. |          |
| P25      | 160.60                                  | ±35.06          | 23.81                              | ±6.82           | 4.24     |
| P90      | 129.96                                  | ±20.86          | 25.91                              | ±3.72           | 4.80     |
| P25/20   | 191.48                                  | ±35.20          | 17.21                              | ±7.71           | 4.12     |

**Fig. 7.** Evolution of phenol photodegradation on P25, P90 and P25/20, at different catalyst concentrations (Lines correspond to fittings from experimental data).

It is noteworthy that when low power irradiation is assumed the proposed kinetic model satisfactorily reproduces the experimental results.

#### 4. Conclusions

An intrinsic kinetic model, able to simulate the behavior of three commercial TiO<sub>2</sub> catalysts with identical chemical structure but with different morphology and hydrodynamic particle size (P25 Aeroxide®, P25/20 VP Aeroperl® and P90 Aeroxide®) has been developed for phenol photocatalytic oxidation process in aqueous suspensions.

The proposed kinetic model takes into account not only the physico-chemical reaction parameters, but also the key parameters related to radiation interaction with these TiO<sub>2</sub> catalysts during the photocatalytic process. As far as the optical coefficients were concerned, lower scattering coefficients were arisen for larger TiO<sub>2</sub> hydrodynamic particle sizes, and consequently lower extinction coefficients were found. Therefore, the effect of TiO<sub>2</sub> hydrodynamic particle size on the optical coefficients has revealed the important role played by this property on the absorbed radiation evaluation.

The performed kinetic model, based on a proposed reaction photo-mechanism, has an explicit dependence on the volumetric rate of photon absorption (VRPA). P25 and P90 catalysts reached their highest VRPA at low catalyst concentrations (0.2 g L<sup>-1</sup>), whereas P25/20 was able to go on absorbing more radiation even when more than 1.0 g L<sup>-1</sup> catalyst concentration was employed. The obtained kinetic model has been successfully validated by experimental data, being able to reproduce the evolution of phenol photodegradation at a wide range of catalyst concentrations for these three studied TiO<sub>2</sub>.

From comparison study of calculated quantum efficiency ( $\eta$ ) as a function of TiO<sub>2</sub> loading, P25 was the most photo-efficient catalyst, whereas P25/20 reached similar efficiencies only when higher TiO<sub>2</sub> concentrations were employed. On the contrary, P90 presented the lowest photo-efficiency with lower photodegradation rates despite absorbing more radiation.

Finally, low irradiation power conditions show a good agreement between predicted and experimental values, with root-square-mean errors below 5%, regardless catalyst concentration or studied TiO<sub>2</sub>.

#### Acknowledgements

This work has been supported by the Spanish Plan Nacional de I+D+i through the project CTM2015-64895-R. Alvaro Tolosana-

Moranchel thanks to Ministerio de Educación, Cultura y Deporte for his FPU grant (FPU14/01605). The authors are also grateful to Technical Research Support Unit of Instituto de Catálisis y Petroleoquímica (CSIC), and Evonik company for TiO<sub>2</sub> samples.

## Appendix A. Derivation of the kinetic model

The derivation of the kinetic model is shown below:

By applying the kinetic steady state approximation, we can obtain HO<sup>•</sup> concentration:

$$\begin{aligned} r_{\cdot OH} &= k_{6a+}[Ti^{IV}(OH)][h^+] + k_{6b+}[Ti^{IV}(H_2O)][h^+] \\ &\quad - k_9[Ti^{IV}|HO^{\cdot}][Ph_{ads}] - k_{10}[HO^{\cdot}][Ph_{ads}] - k_{11}[Ti^{IV}|HO^{\cdot}][Ph] \\ &\quad - k_{12}[HO^{\cdot}][Ph] - \sum_{S=1}^n k_{S,I}[Ti^{IV}|HO^{\cdot}][S_{ads}] + k_{S,II}[HO^{\cdot}][S_{ads}] \\ &\quad + k_{S,III}[Ti^{IV}|HO^{\cdot}][S] + k_{S,IV}[HO^{\cdot}][S] \cong 0 \end{aligned} \quad (1)$$

Furthermore, taken into account:

$$k_{6+} = k_{6a+}[Ti^{IV}(OH)] + k_{6b+}[Ti^{IV}(H_2O)] \quad (2)$$

$$[Ph_{ads}] = K_{3,ph} [site] [Ph] \quad (3)$$

$$[Ti^{IV}|HO^{\cdot}] = K_4 [HO^{\cdot}][Ti^{IV}] \quad (4)$$

Introducing Eqs. (2)–(4) into Eq. (1), it leads to:

$$[HO^{\cdot}] = k_{6+}[h^+]$$

$$\begin{aligned} &/\{(k_9K_4[Ti^{IV}]K_{3,i}[site] + k_{10}K_{3,ph}[site] + k_{11}K_4[Ti^{IV}] + k_{12})[Ph] \\ &+ \sum_{S=1}^n (k_{S,I}K_4[Ti^{IV}]K_{3,ph}[site] \\ &+ k_{S,II}K_{3,I}[site] + k_{S,III}K_4[Ti^{IV}] + k_{S,IV})[S]\} \end{aligned} \quad (5)$$

Defining:

$$\alpha'_{3,ph} = k_9K_4[Ti^{IV}]K_{3,ph}[site] + k_{10}K_{3,ph}[site] - k_{11}K_4[Ti^{IV}] - k_{12} \quad (6)$$

$$\alpha_{3,S} = k_{S,I}K_4[Ti^{IV}]K_{3,ph}[site] + k_{S,II}K_{3,I}[site] + k_{S,III}K_4[Ti^{IV}] + k_{S,IV} \quad (7)$$

Phenol photo-degradation proceeds through a complex scheme of reaction giving rise to intermediate compounds before mineralization is finally reached [16]. Hydroquinone, *p*-benzoquinone (in traces), resorcinol and catechol were detected as first hydroxylation products of phenol with all these TiO<sub>2</sub> catalysts, which undergo further oxidation to yield short organic acids, such as maleic, oxalic, acetic and formic among others. Therefore, taking into account the maximum detected aromatic by-products (hydroquinone, catechol and resorcinol) along photocatalytic reaction was not more than 5.5 ppm, a constant aromatic intermediates concentration was assumed in the kinetic analysis:

$$[HO^{\cdot}] = \frac{k_{6+}[h^+]}{\alpha'_{3,ph}[Ph] + \sum_{S=1}^n \alpha_{3,S}[S]} = \frac{k_{6+}[h^+]}{I(\alpha_{3,ph}[Ph] + 1)} \quad (8)$$

where:

$$I = \sum_{S=1}^n \alpha_{3,S}[S] \quad y \quad \alpha_{3,ph} = \alpha'_{3,ph} / \sum_{S=1}^n \alpha_{3,S}[S]$$

By applying the steady state approximation again in order to obtain hole concentration:

$$r_{(h^+)} = r_g - k_5[h^+][e^-] - k_{(6+)}[h^+] \cong \sim 0 \quad (9)$$

where  $r_g$  is the surface rate of electron-hole generation [28].

Since photo-generation rates of electrons and holes are equal and the semiconductor intrinsic carriers density is comparable low,

we can also make the approximation that  $[h^+] = [e^-]$ . From Eq. (8) we can extract  $[h^+]$  and substitute into Eq. (9) to obtain  $[HO^{\cdot}]$ :

$$[HO^{\cdot}] = \frac{(k_{6+})^2}{2k_5I(\alpha_{3,ph}[Ph] + 1)} \left\{ -1 + \sqrt{1 + \frac{4k_5}{(k_{6+})^2}r_g} \right\} \quad (10)$$

Phenol photodegradation rate per unit catalytic area is expressed by:

$$\begin{aligned} -r_{Ph}^S &= k_9[Ti^{IV}|HO^{\cdot}][Ph_{ads}] + k_{10}[HO^{\cdot}][Ph_{ads}] \\ &+ k_{11}[Ti^{IV}|HO^{\cdot}][Ph] + k_{12}[HO^{\cdot}][Ph] \end{aligned} \quad (11)$$

Substituting Eqs. (3), (4) and (10) into Eq. (11) and rearranging:

$$\begin{aligned} -r_{Ph}^S &= (k_9K_4[Ti^{IV}]K_{3,ph}[site] + k_{10}K_{3,ph}[site] \\ &+ k_{11}K_4[Ti^{IV}] + k_{12})[Ph][HO^{\cdot}] = a_{3,ph}[Ph][HO^{\cdot}] \\ &= \frac{(k_{6+})^2}{2k_5I} \frac{a_{3,ph}[Ph]}{(a_{3,ph}[Ph] + 1)} \left\{ -1 + \sqrt{1 + \frac{4k_5}{(k_{6+})^2}r_g} \right\} \end{aligned} \quad (12)$$

By knowing that the surface rate of electron-hole generation take the form:

$$r_g = \frac{\bar{\phi}e^a}{(S_{BET}C_{cat})} \quad (13)$$

where  $e^a$  correspond to volumetric rate of photon absorption (VRPA) and  $\bar{\phi}$  is the primary quantum yield averaged overall wavelengths. Reaction rate per unit catalytic area is affected by TiO<sub>2</sub> interfacial area per unit suspension volume,  $a_V$ . Then, the reaction rate per unit suspension volume takes the form:

$$\begin{aligned} -r_p &= a_V \frac{(k_{6+})^2}{2k_5I} \frac{\alpha_{3,ph}[Ph]}{(\alpha_{3,i}[Ph] + 1)} \left\{ -1 + \sqrt{1 + \frac{4k_5}{(k_{6+})^2} \frac{\bar{\phi}e^a}{S_{BET}C_{cat}}} \right\} \\ &= S_{BET}C_{cat}\alpha_1 \frac{\alpha_{3,ph}[Ph]}{(\alpha_{3,ph}[Ph] + 1)} \left\{ -1 + \sqrt{1 + \frac{\alpha_2 e^a}{S_{BET}C_{cat}}} \right\} \end{aligned} \quad (14)$$

where  $S_{BET}C_{cat}$  are the TiO<sub>2</sub> specific Surface and the catalyst concentration respectively. Then, in Eq. (14) we have defined:

$$\alpha_1 = \frac{(k_{6+})^2}{2k_5I} y \alpha_2 = \frac{4k_5\bar{\phi}}{(k_{6+})^2}$$

## Appendix A. Supplementary data

Supplementary data associated with this article can be found, in the online version, at <http://dx.doi.org/10.1016/j.apcatb.2016.06.063>.

## References

- J.M. Herrmann, Appl. Catal. B: Environ. 99 (2010) 461–468.
- J. Blanco, S. Malato, Solar detoxification, in: Renewable Energies Series, Unesco Publishing, 2003.
- S. Malato, P. Fernández-Ibáñez, M.I. Maldonado, J. Blanco, W. Gernjak, Catal. Today 147 (2009) 1–59.
- G. Rivas, I. Carra, J.L. García-Sánchez, J.L. Casas-López, S. Malato, J.A. Sanchez-Perez, Appl. Catal. B: Environ. 178 (1) (2015) 210–217.
- A. Mills, J. Wang, D.F. Ollis, J. Catal. 243 (2006) 1–6.
- D.F. Ollis, J. Phys. Chem. B 109 (2005) 2439–2444.
- A. Cabrera-Reina, L. Santos-Juarez, J.L. Sanchez-García, J.L. Casas-López, M.I. Maldonado Rubio, G. LiPuma, J.A. Sanchez-Perez, Appl. Catal. B: Environ. 166–167 (1) (2015) 295–301.
- Transport Theory, in: J.J. Duderstadt, W.R. Martin (Eds.), John Wiley, New York, 1979.
- A. E. Cassano, O. M. Alfano, R. J. Brandi, C. A. Martín, Eliminación de Contaminantes por fotocatálisis Heterogénea, Ed. Digital Graphic, M. A. Blesa (ed.), pp. 201–241 (2001).
- Introduction to X-Ray Power Diffractometry, in: R. Jenkins, R.L. Zinder (Eds.), John Wiley & Sons Inc., New York, 1996.

- [11] S. Brunauer, P.H. Emmet, E. Teller, *J. Am. Chem. Soc.* 60 (1938) 309–319.
- [12] K.M. Reddy, S.V. Manorama, A.R. Reddy, *Mater. Chem. Phys.* 78 (2002) 239–245.
- [13] A.E. Cassano, O.M. Alfano, *Catal. Today* 58 (2000) 167–197.
- [14] M.I. Cabrera, O.M. Alfano, A.E. Cassano, *J. Phys. Chem.* 100 (1996) 20043–20050.
- [15] M.L. Satuf, L.J. Brandi, A.E. Cassano, O.M. Alfano, *Ind. Eng. Chem. Res.* 45 (2005) 6643–6649.
- [16] P. García-Muñoz, J. Carbajo, M. Faraldo, A. Bahamonde, *J. Photochem. Photobiol. A: Chem.* 287 (2014) 8–18.
- [17] J. Carbajo, Thesis Dissertation: Application of Solar Assisted Photodegradation of Organic Pollutants in Aqueous Phase with Nanostructured Titania Catalysts, Universidad Autonoma de Madrid, Spain, 2013.
- [18] H.J. Kuhn, S.E. Braslavsky, R. Schmidt, Chemical Actinometry, IUPAC Tech. Rep. (2004).
- [19] C. Adan, A. Martinez-Arias, M. Fernandez-García, A. Bahamonde, *App. Catal. B: Environ.* 76 (3–4) (2007) 395–402.
- [20] Measurement of Suspended Particles by Quasi-Elastic Light Scattering, in: B.E. Dahneke (Ed.), John Wiley, New York, 1983.
- [21] C. Washington, "Particle Size Analysis in Pharmaceuticals and Other Industries: Theory and Practice", Ed. Ellis Horwood, England (1992).
- [22] W.H. Glaze, J.W. Kang, D.H. Chapin, *Ozone Sci. Eng.* 9 (4) (1987) 335–352.
- [23] R. Brandi, J. Citroni, O. Alfano, A. Cassano, *Chem. Eng. Sci.* 58 (2003) 979–985.
- [24] L. Dombrovsky, D. Baillis, Thermal Radiation in Disperse Systems: An Engineering Approach, Begell House, New York, 2010.
- [25] C.S. Turchi, D.F. Ollis, *J. Catal.* 122 (1990) 178–192.
- [26] O.M. Alfano, M.I. Cabrera, A.E. Cassano, *J. Catal.* 172 (1997) 370–379.
- [27] J. Marugán, R. Van Grieken, A.E. Cassano, O.M. Alfano, *Catal. Today* 129 (2007) 143–151.
- [28] J. Marugán, R. Van Grieken, C. Pablos, M.L. Satuf, A.E. Cassano, O.M. Alfano, *Appl. Catal. B: Environ.* 102 (2011) 404–416.
- [29] M. De los Milagros Ballari, O.M. Alfano, A.E. Cassano, *Ind. Eng. Chem. Res.* 48 (2009) 1847–1858.
- [30] J. Marugán, R. Van Grieken, C. Pablos, M.L. Satuf, A.E. Cassano, O.M. Alfano, *Appl. Catal. B: Environ.* 102 (2011) 404–416.